Acta Materialia 223 (2022) 117447

Contents lists available at ScienceDirect

Acta Materialia

journal homepage: www.elsevier.com/locate/actamat

Dislocation transmission across Σ3{112} incoherent twin boundary: a combined atomistic and phase-field study

Tengfei Ma[a,1], Hyojung Kim[b,1,*], Nithin Mathew[c,1,*], Darby J. Luscher[c], Lei Cao[a], Abigail Hunter[b]

[a] Department of Mechanical Engineering, University of Nevada, Reno, Reno, Nevada 89557, USA
[b] X Computational Physics Division, Los Alamos National Laboratory, Los Alamos, NM 87545, USA
[c] Theoretical Division, Los Alamos National Laboratory, Los Alamos, NM 87545, USA

ARTICLE INFO

Article history:
Received 9 April 2021
Revised 15 October 2021
Accepted 26 October 2021
Available online 3 November 2021

Keywords:
phase field
molecular dynamics
slip transfer
incoherent twin boundary

ABSTRACT

Grain boundaries (GBs) in polycrystalline materials act as impediments to dislocation motion and result in strengthening. Understanding slip transmission through GBs, specifically twin boundaries, is essential to understand the plastic deformation behavior of polycrystalline fcc materials. In this study the interaction between a glide dislocation and Σ3{112} incoherent twin boundary (ITB) in copper is investigated using a combined atomistic and mesoscale approach. The material parameters and structure of the GB in the mesoscale phase field dislocation dynamics (PFDD) model are informed from Molecular Statics (MS) simulations. The structural unit of the ITB consists of an array of three partial dislocations. The interaction between a glide dislocation impinging on each of the GB partial dislocations is investigated using both PFDD and Molecular Dynamics (MD) with two boundary conditions. Transmission planes predicted by both PFDD and MD (NVT) are in agreement, and show that not all transmission events are direct. Critical transmission stresses predicted by PFDD are in the range of 276 MPa to 1380 MPa, while MD predictions are in the range from 100 MPa to 700 MPa. The PFDD and MD predictions of slip transmission are explained using dislocation theory based on isotropic linear elasticity.

1. Introduction

A polycrystalline material's ability to accommodate loading is dependent upon the ease at which dislocations can move through the microstructure to relieve accumulated stress. Grain boundaries (GBs) are the largest impediment to this motion, and consequently it has been well established that GBs provide substantial strengthening in the mechanical behavior of materials [1,2]. Accordingly, there has been a large body of work investigating the strength and ductility of ultra-fine grained materials [3–5] and nano-twinned materials [6–8]. From this work, several possible dislocation-GB interactions have been observed in experiments and by atomistic simulations [9–12], including slip transfer, where a dislocation can transmit through a GB, or absorption of a dislocation, followed by glide along the GB, and then re-emission, possibly with an altered character. When there is particularly poor alignment between grains, dislocations can pile-up against GBs causing localized stress concentrations, which can contribute to work hardening [2,13,14]. Hence, it is not surprising that dislocation-GB interactions have been shown to play an important role in the mechanical response of metals and alloys, not just in the yield strength and work hardening behavior, but also in damage nucleation and propagation and fracture resistance [15–19].

Whether or not a dislocation can transmit through a GB is highly dependent on the orientation between grains, and more specifically how well aligned the slip systems are between grains [12,20–22]. A general GB can be geometrically represented with five macroscopic degrees of freedom and three microscopic degrees of freedom [23]. Several GB geometry based criteria have been proposed [10,24] to characterize the ease of dislocation transmission. In consideration of just these macroscopic degrees of freedom alone, one can see that the number of possible GBs is large. Hence, it is difficult to verify geometric criteria generally. Even Molecular Dynamics (MD) has been applied to investigate only a small subset of the possible GB structures [10]. Furthermore, it is not yet clear which geometric degrees of freedom are most important to include in continuum-scale criteria, and which, if any, can be neglected. Consequently, many of the geometric criteria do not compare well with experimental data and/or are limited in applicability to specific types of GBs [24].

* Corresponding authors.
E-mail addresses: hkim3@lanl.gov (H. Kim), mathewni@lanl.gov (N. Mathew).
[1] These authors contributed equally to this work.

https://doi.org/10.1016/j.actamat.2021.117447
1359-6454/

Of the vast number of possible GBs, twin boundaries are particularly common in face-centered cubic (fcc) metals due to their low formation energy [25–28]. Consequently, there have been many atomistic and experimental studies of coherent twin boundaries (CTB) [11,29–33], and also incoherent twin boundaries (ITB) [34–38]. Various interaction mechanisms have been suggested regarding the glide dislocation interaction with TBs, such as pile-up at GB, absorption, direct transmission and cross-slip event depending on the TB configurations, types of incoming dislocation, and the applied stress state [35,37,39–44]. For example, in nanocrystalline metals, CTBs have been shown to have particular resistance to slip transfer events [11,30,33,45–48], and this barrier to dislocation transmission is largely responsible for the high strength of nanotwinned materials [6,49–51]. On the other hand, Liang *et al.* [36] reported that screw glide dislocations in Cu can transmit across CTBs that make up 3D annealing twins, and then cross-slip by dislocation looping. This causes dislocation annihilation in between the upper and lower bounding CTB. ITBs are typically less common than CTBs, but are comprised of Shockley partial dislocations that can move under externally applied stresses causing GB migration, and thus are associated with detwinning [52]. Hence, ITBs can influence plastic deformation in nanocrystalline materials as well, and much of the research addressing ITBs has focused on the migration and propagation of these boundaries rather than dislocation-GB interactions. Despite this, slip transfer through ITBs has been observed experimentally during *in situ* nano-indentation studies [37,38].

There have been several modeling studies addressing slip transmission through ITBs, however, most of these studies have been completed using MD [31,35–37,53,54]. Also, most of these studies have not investigated thoroughly the effect of where the initial glide dislocation plane impinges upon the GB dislocation array on transmission behavior, including the effect on the transmission plane and critical transmission stress, in particular for Cu. Despite the ability of atomistic approaches to capture many dislocation-GB interactions, they are still limited to small time steps, high loading rates, and relatively small length scales. It is also often difficult to understand specific interaction events using MD due to the ubiquitous presence of complex interactions. The ability to connect deformation mechanisms to dislocation theory is important to the development of physically informed continuum models at macrosopic scales. At macroscopic length scales, modeling of the detailed interactions between GBs and other defects is impossible due to the immense computational cost that arises with such an approach (hence the utility of geometric criteria discussed previously). In particular, the effect of dislocation cores and stacking faults are often neglected at this scale. To address these issues, there has been much effort in the development of mesoscale approaches to both fill the gap between atomistic and continuum scales and faithfully bridge between the scales. Clearly, understanding dislocation-GB interactions, and their impact on overall material response is a multiscale problem.

To our knowledge, there have been no mesoscale modeling approaches utilized to study dislocation-GB interactions in ITBs. However, there have been efforts to investigate such interactions for other GBs, and thus these approaches could in principle be applied to study ITBs. For example, quasi-continuum approaches, such as Coupled Atomistic/Discrete Dislocation (CADD) [53,55,56] and Concurrent Atomistic-Continuum (CAC) [33], along with Discrete Dislocation Dynamics (DDD) [57–60] models have been used to study slip transmission across GBs. More specifically, DDD approaches have been primarily used to address dislocation transmission through low-angle GBs [58,59,61], and CAC has modeled the sequential slip transfer through CTBs [33]. However, DDD does not represent the dislocation misfit energy, such as the stacking fault energy and detailed core structures, which impacts the interaction between glide dislocations and GBs that often also consist of dislocations. Coupled atomistic approaches, such as CADD and CAC, provide accurate descriptions of dislocation-GB interactions, but, similar to MD, it can be difficult to decouple and understand specific interaction mechanisms.

Other applicable mesoscale modeling techniques include phase-field (PF) based methods used to describe dislocation dynamics. While such approaches have not previously been applied to address slip transfer through GBs, they have been employed to model dislocation transmission through bimetal interfaces [62,63]. These approaches evolve dislocation configurations by minimizing the total energy, which generally describes elastic interactions between dislocations, effects of the dislocation core and stacking fault regions, and interactions of the dislocations with respect to applied stress [64–66]. Thus, dislocation structure, motion, interactions, and reactions occur based on the most energetically favorable pathway, and are not governed by *a priori* selected guiding criteria. Similar to other mesoscale approaches, PF methods discretely resolve dislocations. Hence, a GB can be explicitly represented by the misfit structure it is comprised of, and specific interactions between misfit dislocations and gliding dislocations can be studied, assuming that the structure of the GB is known *a priori*. This is the approach taken in this work to study dislocation interactions with an ITB in copper. Since the GB misfit structure must be known *a priori*, we employ MS simulations to both inform this structure, along with other structural parameters and needed generalized stacking fault energies. MD simulations are also used to provide a comparative study of the transmission behavior in detail. Combined with the mesoscale PF simulations, we can begin to connect different transmission behaviors to dislocation theory, and decouple the effects of elasticity and dislocation core interactions.

In this work, we specifically address dislocation slip transmission behavior in an ITB using MD and a PF model called Phase Field Dislocation Dynamics (PFDD). $\Sigma 3$ {112} ITBs have been shown to have a repeating structure of three partial dislocations, each on a {111} plane [34]. Here we utilize both MD and PFDD simulations to study the interaction of gliding partial dislocations (of mixed type) with the misfit dislocations comprising a $\Sigma 3$ {112} ITB in copper. Interestingly, the results from both MD and PFDD show that the transmission process is dependent on where along the GB the partial dislocation intersects. In addition, in some cases the transmission process is not a direct one, and the transmitting dislocation emits on a neighboring plane. The cause of this is discussed and explained using dislocation theory.

The remainder of the paper is organized as follows. Section 2 briefly reviews both the atomistic and mesoscale modeling approaches adopted in this study, with particular focus on how the ITB is represented. Next, Section 3 presents and compares the simulation results. Based on these results, Section 4 discusses the underlying mechanisms resulting in the slip transmission behavior observed in the simulations. For example, transmission behavior is computed using both isotropic and anisotropic elasticity within PFDD, which is then compared to dislocation theory and MD results. Concluding remarks are given in Section 5.

2. Methods

In this section we first present the details of the Molecular Dynamics (MD) simulations and Molecular Statics (MS) calculation of material properties required to inform the PFDD simulations, including the stiffness tensor, lattice parameter, and Generalized Stacking Fault Energy (GSFE) curves. Next, we present a brief overview of the PFDD approach. In particular, this section describes how the GB dislocations are accounted for and details of the simulation set-up within this model framework.

Table 1
Material parameters including the lattice parameter a, the intrinsic stacking fault energy E^{isf}, and lattice elastic constants calculated from MS simulations and were used to inform the PFDD model. Isotropic elastic moduli (shear modulus μ and bulk modulus K) were calculated using the Voigt average. All elastic constants are in units of GPa.

C_{11}	C_{12}	C_{44}	a (Å)	μ	K	E^{isf} (mJ/m^2)
169.9	122.6	76.2	3.615	55.2	138.4	44.4

2.1. Molecular Dynamics

All MD and MS simulations were performed using the LAMMPS [67] software. The Embedded Atom Method (EAM) potential for Cu developed by Mishin *et al.* [68] was used in the simulations. The stiffness tensor for linear elasticity (C_{ijkl}) was calculated using MS simulations with a 3D periodic simulation cell, with 6 repeat units in the Cartesian directions x, y, z oriented along the [100], [010], and [001] crystallographic directions, at equilibrium geometry corresponding to P = 0 atm and T = 0 K. This simulation cell was affinely deformed using a prescribed set of lattice strains (-0.05% to 0.05% in steps of 0.01%). The C_{ijkl} were obtained from these deformed geometries using energy-strain curves, and are reported in Table 1 along with the corresponding isotropic Voigt averages. The GSFE surface (i.e., the γ-surface with a grid spacing of 0.05 Å) was calculated using the standard procedure [69,70] in which, relaxation of atoms are allowed only in the direction normal to the glide plane (111) and periodic boundary conditions are used only in the glide plane. The intrinsic stacking fault energy, E^{isf}, is the energy of the stacking fault along $< 112 >$, and is also reported in Table 1. The predicted values are in good agreement with reported values in literature for the same interatomic potential.[68,71]

We also performed MD simulations to provide a basis for comparison with PFDD simulations of the interactions between a dislocation and an ITB. The simulation cell for the GB-dislocation interaction consisted of 2,721,600 atoms and was of the approximate dimensions 56.4 nm, 111.6 nm, and 5.1 nm in the x, y, and z Cartesian directions, corresponding to $[11\bar{1}]$, [112], and $[1\bar{1}0]$ in Crystal 2 and $[\bar{1}\bar{1}\bar{1}]$, $[11\bar{2}]$, and $[1\bar{1}0]$ in Crystal 1. Periodic boundary conditions were applied in the three Cartesian directions, resulting in two GBs. The initial structure for the ITB was prepared using the method prescribed by Tschopp *et al.*[72] and had an excess energy of 592 mJ/m^2 after energy minimization. This value is in good agreement with the value reported in literature [34]. To study the interaction of the ITB with screw dislocations, a screw dislocation dipole (80 $|\mathbf{b}|$ apart), was placed in the center of one of the crystals using the isotropic linear elastic solution for the displacement field of a dislocation dipole. The dislocations were driven to the ITB by two methods: (1) affine deformation of the simulation cell followed by simulations in the canonical (NVT) ensemble at 1 K (denoted as MD-NVT) and (2) affine deformation of the simulation cell followed by simulations in the iso-thermal iso-baric (NPT) ensemble at 1 K (denoted as MD-NPT). For the affine deformation, the strain to be applied to the simulation domain was calculated using linear anisotropic elasticity and the specified stress tensor ($\sigma_{<111><111>}$, $\sigma_{<112><112>}$, $\sigma_{<110><110>}$, $\sigma_{<111><112>}$, $\sigma_{<112><110>}$ =0 and $\sigma_{<111><110>}$ =Resolved Shear Stress). Although the initial stress state in MD-NVT was close to the targeted state, $\sigma_{<111><110>}$ drops and $\sigma_{<112><110>}$ increases once the dislocation gets close to the GB, possibly due the GB-dislocation interaction and shearing of the GB, as shown in the appendix (Fig. A.1) for a representative case of the b_1-plane. Therefore, we performed the MD-NPT simulations to compare with MD-NVT. A Nose-Hoover thermostat was applied with the coupling parameter set to 100 fs for the NVT simulations. NPT simulations were performed with the temperature damping set to 100 fs and pressure damping set to 1000 fs. Independent simulations were performed for each stress value.

2.2. Phase Field Dislocation Dynamics (PFDD)

The PFDD approach relies on development of the total system energy. The energy of the system is formulated such that changes in the energy due to individual dislocation motion can be accounted for. In this work, we consider three key energy terms [64,73]:

$$E = E^{strain} + E^{core} - E^{ext} \tag{1}$$

where E^{strain} is the elastic strain energy that accounts for dislocation-dislocation interactions, E^{core} describes the energy required for a perfect or partial dislocation to move through the crystal lattice, breaking and reforming atomic bonds, including the formation or presence of a stacking fault, and E^{ext} is the external energy term that accounts for interactions between dislocations and the applied stress.

Within the PFDD approach, the motion and interaction of individual dislocations are accounted for through the evolution of order parameters, or phase field variables, $\xi_\alpha(\mathbf{x}, t)$. While each order parameter is a scalar-valued variable, they are associated with the slip direction and slip plane normal of the active slip systems, α, of interest during a simulation. Integer jumps in the order parameters indicate the location of a perfect dislocation, and fractional values of the order parameters indicate partial dislocations. For example, a single fcc crystal could have 12 active order parameters, each corresponding to a $< 110 >$ type slip direction on the {111} slip planes. In this work, we consider glide of a screw dislocation in Cu on a (111) plane. This requires three active order parameters, linear combinations of which allow the perfect screw dislocation to dissociate into a leading and trailing partial dislocation with a stacking fault in between. We include three additional order parameters to represent the boundary dislocations. These details are discussed further in Section 2.2.1

It is assumed that plastic strain is mediated by the motion and interaction of dislocations, and is thus directly dependent upon the order parameters [64,65]:

$$\epsilon^p_{ij}(\mathbf{x}, t) = \frac{1}{2}\sum_{\alpha=1}^{N} \frac{|\mathbf{b}_\alpha|}{l_\alpha}\xi_\alpha(\mathbf{x}, t)\left(s^\alpha_i m^\alpha_j + s^\alpha_j m^\alpha_i\right) \tag{2}$$

where $|\mathbf{b}_\alpha|$ is the Burgers vector magnitude, l_α is the interplanar distance, s^α_i is the slip direction, m^α_j is the slip plane normal, and N is the total number of active slip systems, where each slip system is indicated by α. Using Eq. (2), the elastic strain energy can be formulated to directly depend on the order parameters [64–66]:

$$E^{strain} = \frac{1}{(2\pi)^3}\fint \frac{1}{2}\hat{A}_{mnuv}(\mathbf{k})\hat{\epsilon}^p_{mn}(\mathbf{k})\hat{\epsilon}^{p*}_{uv}(\mathbf{k})d^3k \tag{3}$$

where a superposed ($\hat{}$) denotes the Fourier transform, $\hat{A}_{mnuv}(\mathbf{k}) = C_{mnuv} - C_{kluv}C_{ijmn}\hat{G}_{ki}(\mathbf{k})\mathbf{k}_j\mathbf{k}_l$, $\mathbf{k}_i$ is the wavenumber vector, $\hat{G}_{ki}(\mathbf{k})$ is the Fourier transform of the Green's tensor of linear elasticity, C_{ijkl} is the elastic moduli tensor, $\fint$ denotes the principal value of the integral, and the superscript (*) denotes the complex conjugation. In the simulations discussed below, we account for cubic anisotropic elasticity unless otherwise mentioned, and the details of the implementation of the full anisotropic tensors are discussed in [74]. We also present a comparison of the PFDD results employing anisotropic elasticity with corresponding results from simulations in which isotropic elastic behavior is assumed. Table 1 presents the elastic constants and isotropic shear and bulk moduli, which were determined using a Voigt average of the cubic elastic constants, used in our simulations.

Table 2
Coefficients used in Eq. (6). Values were directly informed from MS calculations described in Section 2.1. All units are in mJ/m^2.

c_0	c_1	c_2	c_3	c_4	a_1	a_3
320.31	-73.07	-46.28	13.36	-0.27	-107.92	-22.90

Similar to the elastic strain energy, the external energy term can also be presented as a function of the order parameters [64–66] via the expression:

$$E^{ext} = \int_V \sigma_{ij}\epsilon^p_{ij}(\mathbf{x},t)d^3x \tag{4}$$

where σ_{ij} is the applied stress tensor.

The core energy depends on the material and corresponding crystallography under consideration, hence there have been many functional forms, and also tabular input, used previously [64,73,75,76]. Most broadly this term can be expressed as:

$$E^{core} = \sum_{\beta=1}^{N_p} \int \frac{1}{l_\beta}\phi_\beta(\xi_1(\mathbf{x}),\xi_2(\mathbf{x}),...,\xi_N(\mathbf{x}))d^3x \tag{5}$$

where $\phi_\beta(\xi_1,\xi_2,...)$ is a periodic potential that may be a function of one or more order parameters. This potential is integrated over the slip plane, β, for the total number of active slip planes, N_p. For gliding dislocations in this study, we chose to use a complex Fourier series approximation of the material γ-surface [77,78].

$$\begin{aligned}\phi_\alpha(\xi_1,\xi_2,\xi_3) = {} & c_0 + c_1[\cos 2\pi(\xi_1-\xi_2)+\cos 2\pi(\xi_2-\xi_3)+\cos 2\pi(\xi_3-\xi_1)]\\ & +c_2[\cos 2\pi(2\xi_1-\xi_2-\xi_3)+\cos 2\pi(2\xi_2-\xi_3-\xi_1)+\cos 2\pi(2\xi_3-\xi_1-\xi_2)]\\ & +c_3[\cos 4\pi(\xi_1-\xi_2)+\cos 4\pi(\xi_2-\xi_3)+\cos 4\pi(\xi_3-\xi_1)]\\ & +c_4[\cos 4\pi(3\xi_1-\xi_2-2\xi_3)+\cos 4\pi(3\xi_1-2\xi_2-\xi_3)+\cos 4\pi(3\xi_2-\xi_3-2\xi_1)\\ & +\cos 4\pi(3\xi_2-2\xi_3-\xi_1)+\cos 4\pi(3\xi_3-\xi_1-2\xi_2)+\cos 4\pi(3\xi_3-2\xi_1-\xi_2)]\\ & +a_1[\sin 2\pi(\xi_1-\xi_2)+\sin 2\pi(\xi_2-\xi_3)+\sin 2\pi(\xi_3-\xi_1)]\\ & +a_3[\sin 4\pi(\xi_1-\xi_2)+\sin 4\pi(\xi_2-\xi_3)+\sin 4\pi(\xi_3-\xi_1)]\end{aligned} \tag{6}$$

This equation has been used previously to model perfect dislocations in fcc metals that dissociate into two partial dislocations surrounding a stacking fault region [73,79–81]. Note, this equation is written for only one glide plane with three active order parameters, which corresponds to the case considered here. The three order parameters, ξ_1, ξ_2 and ξ_3, are defined in perfect dislocation directions (i.e., $[01\bar{1}]$, $[1\bar{1}0]$ and $[\bar{1}01]$, respectively) for fcc materials, hence the linear combinations of all three on an active slip plane are required in order to model partial dislocation directions also active on the same slip plane[78]. Thus, the dissociation of perfect dislocation $1/2[\bar{1}10] \rightarrow 1/6[\bar{1}2\bar{1}] + 1/6[\bar{2}11]$ is expressed in terms of order parameters as, $\xi_2 \rightarrow 1/3(\xi_1-\xi_2)+1/3(-\xi_2+\xi_3)$. Here ξ_2 describes a perfect dislocation aligned to the y-axis and the linear combination of ξ_1 and ξ_2 describes the leading partial, while the linear combination of ξ_3 and ξ_2 describes the trailing partial dislocation.

The seven coefficients $c_0, c_1, c_2, c_3, c_4, a_1, a_3$ define the overall shape of the approximated γ-surface, including the material-dependent local minima, maxima, and 2D curvature. Determination of these coefficients require information about the material γ-surface calculated with atomistic methods. This determination of these coefficients and corresponding quality of the approximated γ-surface have been discussed in detail in previous work for fcc metals [73,78–80], hence it is not revisited here. In this work, the coefficients are informed using values from the γ-surface calculated with MS. More details are included in Section 2.1, and the coefficients are presented in Table 2.

Finally, the evolution of the dislocation system (via the order parameters, $\xi_\alpha(\mathbf{x})$) is driven by the time-dependent Ginzburg-Landau equation.

$$\frac{\partial\xi_\alpha(\mathbf{x})}{\partial t} = -L\frac{\delta E}{\delta\xi_\alpha(\mathbf{x})} \tag{7}$$

where E is the total energy of the system and L is the kinetic coefficient that relates to the dislocation mobility [20].

2.2.1. Modeling Boundary Defects

To explicitly represent the GB within the PFDD calculations, we introduce a set of stationary (immobile) misfit dislocations via specification of an additional set of three active order parameter fields. Here we focus on dislocation interactions with a $\Sigma3$ {112} ITB seen experimentally in Cu [34,82,83]. This boundary has been shown to have two possible structures, where the lowest energy structure comprises a repeating structure of three partial dislocations, each on a {111} plane [34]. The three partial dislocations include one pure edge partial, and two mixed-type partial dislocations with equal and opposite screw components. Hence, the net sum of the Burgers vectors of these three partials is zero.

Since the boundary dislocations are all partial dislocations, their order parameters are defined to represent the partial slip directions, resulting in different treatment in the core energy calculations from glide dislocations. These partial dislocations do not have a subsequent leading/trailing partial dislocation, or bound a stacking fault since they are misfit dislocations within the boundary. The corresponding dissociation of a perfect dislocation does not need to be modeled to create these dislocations, and therefore, linear combinations of the three perfect-type order parameters do not need to be accounted for in E^{core} for these order parameters. Hence the periodic potential used for the boundary dislocations is defined as:

$$\phi_\beta(\xi_\alpha) = E^{isf}\sin^2(\pi\xi_\alpha(\mathbf{x},t)) \tag{8}$$

where E^{isf} is the intrinsic stacking fault energy calculated from the MS simulations. The value is provided in Table 1. Note that these GB partial dislocations are incorporated in the elastic energy (see Eq. (2)) with Burgers vectors that are different from a perfect dislocation.

2.3. Simulation Set-up

All PFDD simulations were carried out in a 3D rectangular simulation cell, shown in Fig. 1(a), with periodic boundary conditions in all directions, which are a consequence of the Fourier transform in the calculation of the elastic strain energy. The simulation cell is comprised of two different grains, which we refer to as Crystal 1 and Crystal 2. The simulation cell is 105nm × 3nm × 15nm using a computational grid of 504 × 12 × 72. The grid spacing is chosen as the z-direction interplanar spacing i.e., l_α for all directions.

Fig. 1(a) shows the location of two ITBs, indicating that the simulation cell has two regions that correspond to Crystal 1, and one central region that corresponds to Crystal 2. As mentioned, the $\Sigma3$ {112} ITB of interest in this work consists of a set of partial dislocations with repeatable sequences b_2:b_1:b_3 where b_1, b_2 and b_3 are equal to $\frac{1}{6}[11\bar{2}]$, $\frac{1}{6}[\bar{2}11]$ and $\frac{1}{6}[1\bar{2}1]$, respectively [34].

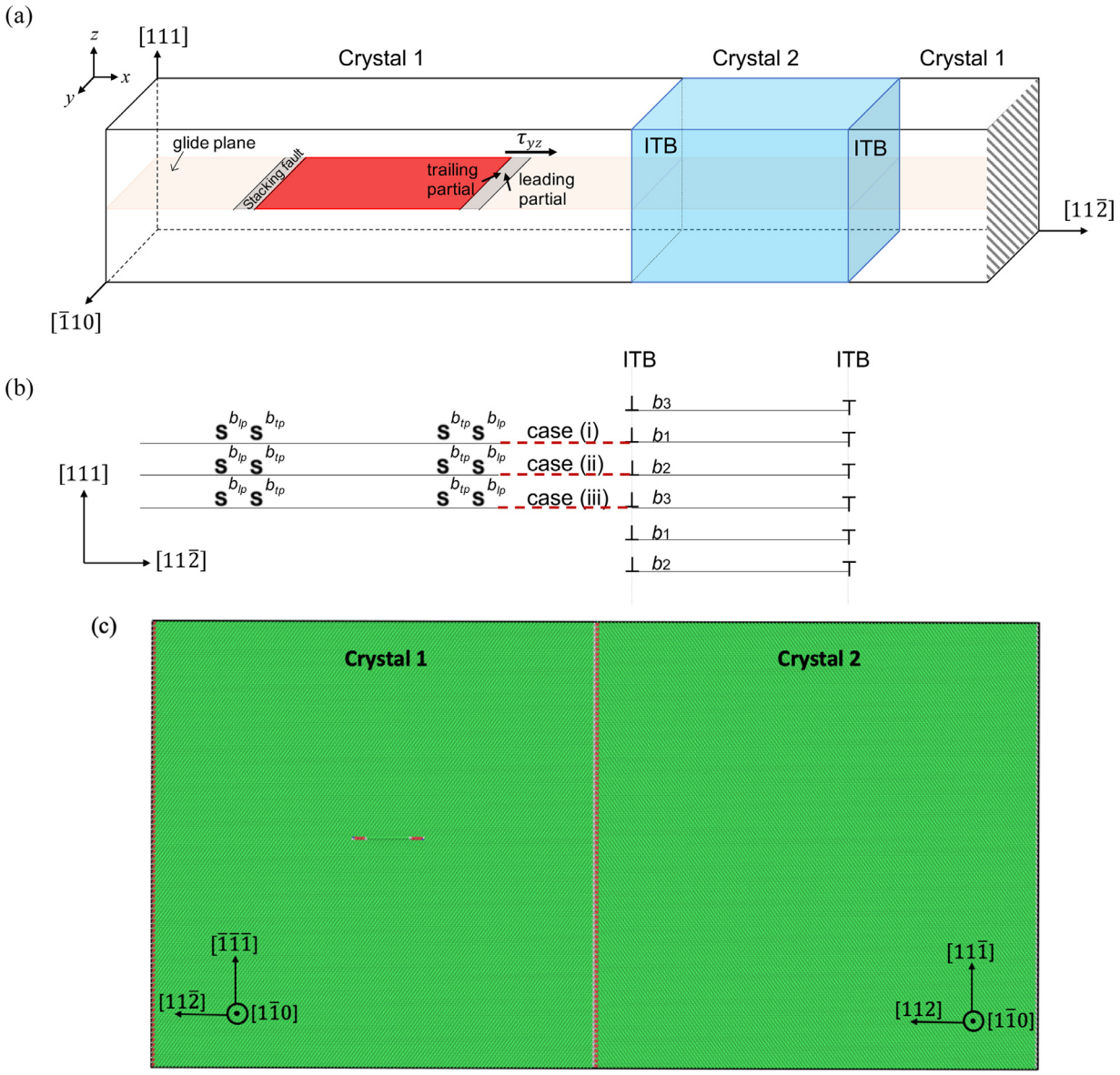

Fig. 1. (a) A schematic of the PFDD simulation cell showing three grains distinguished by two inverse Σ3{112} ITBs. The leading and trailing partial dislocations move toward the ITB under the applied stress τ_{yz}. (b) Three possible glide planes are shown with respect to the dislocation arrays in Σ3{112} ITBs, which are indicated using dislocation symbol, ⊥. The gliding dislocation, a perfect screw dipole, is placed on the left side of the simulation cell in Crystal 1 and relaxed into partial dislocations (i.e., leading partial as $\mathbf{s}^{b_{lp}}$ and trailing partial as $\mathbf{s}^{b_{tp}}$, respectively). The Σ3{112} ITB consists of the repeating three partial dislocations (i.e., b_1, b_2 and b_3) array in Crystal 2. We considered all three cases where the glide plane in Crystal 1 is on the b_1-,b_2- and b_3- plane, respectively. (c) Schematic of the MD simulation cell with atoms colored according to adaptive-Common Neighbor Analysis (CNA) as implemented in OVITO [84,85]. The colors represent the following: Green for FCC, magenta for HCP, blue for BCC, and white for unidentified. The vertical row of magenta and white atoms represents the GB. The dissociated dipole can be seen on the left side of the GB.

Each dislocation is placed on the appropriate plane in repeating b_3, b_1, b_2 triples. The system is then relaxed for 50 time steps, so that the initial input step function in the order parameter can form a smooth transition across the dislocation line. This transition is representative of the core region of the boundary partial dislocations. The plane on which there is a partial of b_1 (b_2 or b_3) in the ITB will henceforth be referred to as b_1 (b_2 or b_3) plane for simplicity. Fig. 1(b) shows the representation of three possible dislocation configurations with the Σ3{112} ITB in which different glide planes are considered in the PFDD simulations. In case (i), the gliding partials are initially located on the b_1 plane, and hence, move along the b_1 plane under stress until the leading partial dislocation reaches the ITB. Similarly, case (ii) and case (iii) initially locate the gliding dislocations on the b_2- and b_3 plane, respectively. Both a positive and negative ITB is defined within the simulation cell (see ITBs in Fig. 1(b)), so that the entire computational cell has a net zero Burgers vector.

Fig. 1 also shows that a perfect screw dislocation dipole with a Burgers vector of $[\bar{1}10]$, is placed on the glide plane in the left side of the simulation cell, in Crystal 1. This glide dislocation is relaxed into partials under no stress, where $\frac{1}{6}[\bar{1}2\bar{1}]$ and $\frac{1}{6}[\bar{2}11]$ are the leading partial and trailing partial Burgers vectors respectively. We note that in this work, the leading partial is defined as the partial dislocation closest to the ITB, and the trailing partial is the subsequent dislocation bounding the stacking fault region. This geometry is combined with the boundary dislocations, which have already been relaxed. A constant shear stress, τ, is then applied to the system to drive the gliding dislocation toward, and eventually through the ITB for each case shown in Fig. 1(b). The applied stress in each simulation is incremented by 0.005μ in order to de-

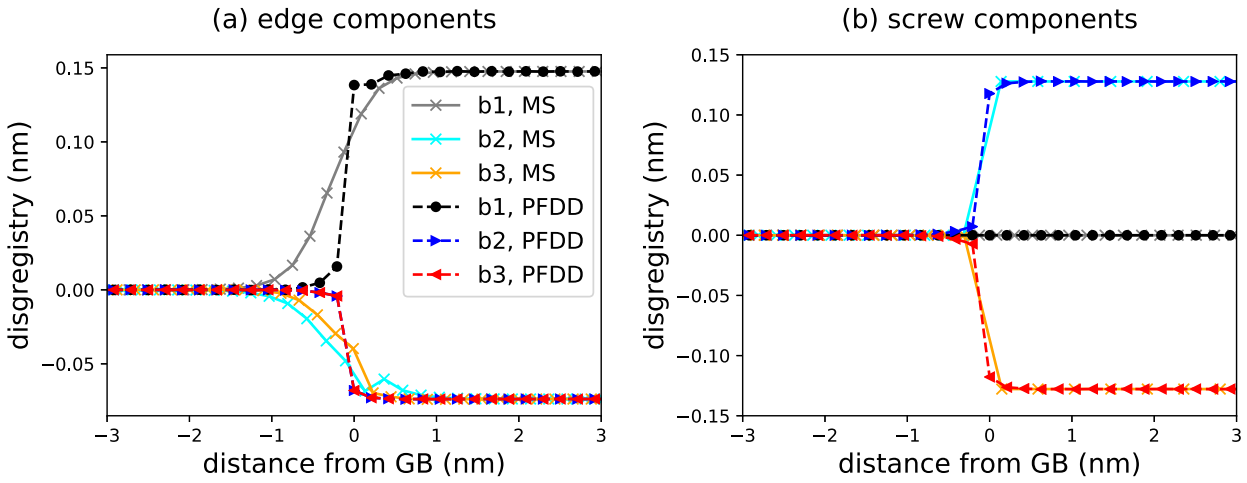

Fig. 2. Comparison of the (a) edge and (b) screw components of the disregistry across the Σ3{112} ITB as calculated with MS and PFDD simulations.

termine the critical stress required for the gliding dislocation to transmit across the ITB. If the gliding dislocation fails to transmit across the ITB in the simulation at one applied stress and the simulation reaches convergence with the tolerance of 10^{-4}, the stress is incremented (increased). Once the dislocation transmits, we consider the critical stress to be between the current stress value, and the previous increment.

3. Results

In this work, we conduct PFDD and MD simulations to investigate the transmission behavior of a pure screw dislocation across a Σ3{112} ITB. First, the disregistry of the ITB predicted by PFDD and MD are compared. Then the transmission processes are demonstrated and the critical stresses for successful transmission are presented.

3.1. Disregistry analysis of the twin boundary

Before considering the interaction of a gliding dislocation with the ITB, we first compare the boundary structure between MS and PFDD. In the PFDD model, we computed the disregistry projected along the β direction (which is either parallel or normal) to the dislocation line as below:

$$\text{disregistry}_\beta = \sum_{\alpha=1}^{3} \xi_\alpha b_\alpha \cdot s_\beta, \tag{9}$$

where ξ_α is αth order parameter, and s is the slip direction. The disregistry calculation in MS simulations follows the methodology in reference [86]. In this method, pairs of atoms, which straddle the plane of the GB dislocation, are first identified in a reference configuration (Crystal 2 in this case). The displacements between these atoms are calculated in the deformed configuration (ITB in this case) and the reference configuration. The difference between displacements gives the disregistry.

Fig. 2 shows a quantitative comparison of the edge and screw components of the disregistry of the relaxed b_1, b_2, and b_3 boundary dislocations along the ITB as calculated with PFDD and MS. Fig. 2(a) shows the edge components (along $< 112 >$ direction) and Fig. 2(b) shows the screw components (along $< 110 >$ direction) of the disregistry. The character types of the boundary dislocations can be clearly seen in these figures. As mentioned previously, b_1 is of pure edge type, and hence, has zero disregistry in the $< 110 >$ direction. In addition, Fig. 2(b) shows that b_2 and b_3 have equal and opposite screw components. Fig. 2(a) shows that b_2 and b_3 have equal edge components, but both are opposite in sign to b_1. It can be clearly seen how the three Burgers vectors sum to a zero net Burgers vector when a circuit is taken over a triad of boundary dislocations.

The disregistry predicted by PFDD and MS simulations shows good agreement, particularly in the case of the screw components, which show near perfect agreement. PFDD simulations predict that the edge components of the b_2 and b_3 partials perfectly overlap, while MS simulations predict a slight difference between b_2 and b_3 partials (Fig. 2(a)). In addition, the MS simulations predict more diffuse disregistry than PFDD does for the edge components. The narrower core structure is expected for this PFDD formulation, which does not include a gradient energy term [87]. A gradient energy term could be included in PFDD simulations, but would require additional fitting to MS simulations and is dependent on the dislocation character. For simplicity we omit this contribution here. Finally, the current PFDD model inherently couples the degree of relaxation for screw and edge components of mixed partial dislocations, while MS allows decoupled relaxation of edge or screw components. This may also be a source of the differences seen in the disregistry of the edge components.

3.2. Transmission of a screw dislocation across the ITB: Crystal 1 to Crystal 2

Both MD and PFDD simulations were performed to study how a screw dislocation interacts with and transmits across the Σ3{112} ITB. As described previously, the perfect screw dislocation immediately dissociates into two partial dislocations in Cu. Thus, the dislocation-GB interaction in these simulations is predominately between the leading partial dislocation and the ITB. As described previously in Section 2.2 and shown in Eq. 6, linear combinations of the three active order parameters (defined in perfect dislocation slip directions) are used to model the partial dislocations. However, it is not straightforward to visualize the gliding partials because of how they are represented. In order to clearly visualize the gliding dislocation evolution in the PFDD simulations, we plot the vector projection of the order parameters in the perfect screw slip direction, as shown in Eq. (10) [78,80,88] where $\mathbf{s}^\alpha$ are the slip directions (normalized Burgers vector direction), and $\mathbf{s}_{scr}$ is the slip direction of the perfect screw direction.

$$d_{slip}(\mathbf{x}) = \sum_{\alpha=1}^{3} \xi_\alpha(\mathbf{x})\, \mathbf{s}^\alpha \cdot \mathbf{s}_{scr} \tag{10}$$

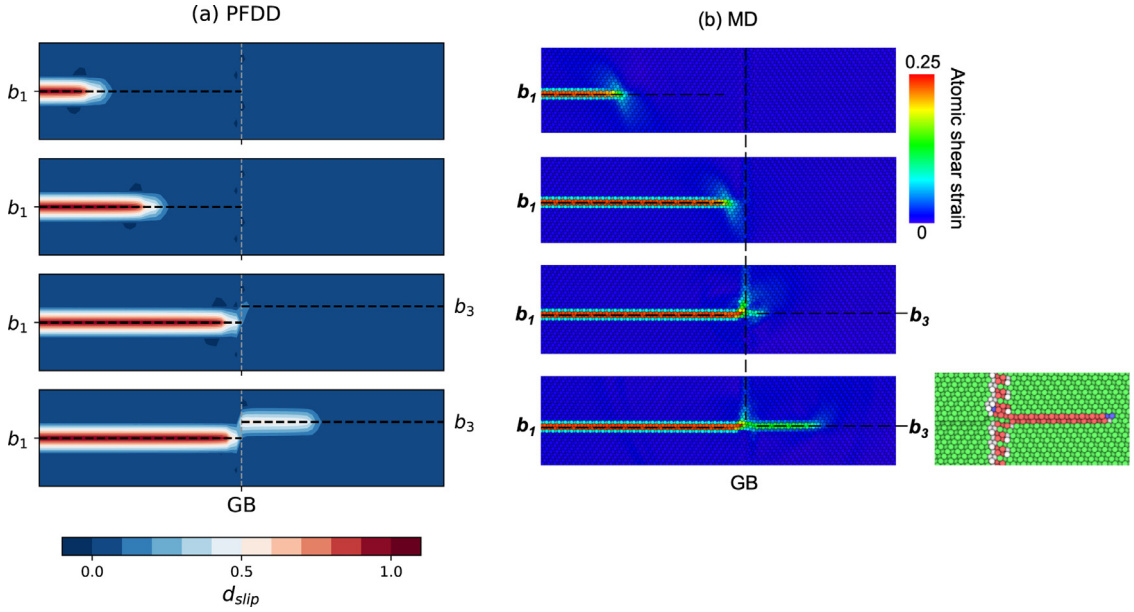

Fig. 3. (a) PFDD and (b) MD-NVT simulations of transmission of a dissociated screw dislocation dipole on a (111) plane that is aligned with the b_1 boundary dislocation. Also shown is the adaptive-CNA representation of atomic structure after transmission. With increasing time (from top to bottom figure) under stress, the leading partial dislocation transmits onto a different (111) plane, which is aligned with the b_3 boundary dislocation. For PFDD, the same magnitude of stress is applied for the top three figures and increased by 0.005μ for the bottom figure to enable transmission.

Fig. 3(a) shows the PFDD-computed transmission process when the initial screw dislocation dipole is placed on the (111) plane aligned with the b_1 plane. From the initial configuration shown in Fig. 3(a)(top), the initial screw dislocation dipole has dissociated creating a stacking fault region (white region at the tip of the red region). Once an equilibrium stacking fault width is reached, the leading and trailing partial dislocations propagate toward the boundary. When the leading partial meets the boundary, there is initially not enough stress for transmission to occur. Hence, the leading partial stops at the ITB. As the applied stress is increased, the trailing partial moves closer to the leading partial, decreasing the width of the stacking fault. Once a critical stress level is reached, the leading partial dislocation transmits through the ITB into Crystal 2, and the trailing partial remains arrested at the ITB in Crystal 1, as shown in Fig. 3(a)(bottom). An interesting result apparent in Fig. 3(a)(bottom) is that the leading partial dislocation does not transmit directly across the ITB, but rather exits the boundary on the b_3-plane.

The MD-NVT simulations exhibit similar dislocation interaction and transmission behavior. Fig. 3(b) shows the transmission behavior of leading and trailing partial dislocations from the MD-NVT simulations. The atoms in Figs. 3 and 4 are colored according to the local atomic shear strain invariant (von Mises) [89,90]. Similar to the PFDD results, the leading partial dislocation transmits through the ITB, and emerges on the b_3-plane. Converse to the PFDD results, the MD results show that the trailing partial dislocation enters the GB and glides in the interface plane, however, it quickly arrests and ultimately does not propagate far. This type of transition in glide plane, resulting in glide of the trailing partial along the GB plane, is not yet accounted for in PFDD, hence Fig. 3(a)(bottom) shows that once the leading partial transmits into Crystal 2 and continues to glide, the trailing partial remains arrested at the ITB on the b_1 plane in Crystal 1.

Because the ITB has a repeating structure of three different partial dislocations, the interaction between the gliding dislocation and GB will be different depending on where the gliding dislocation impinges on the boundary. A different interaction could also correspond to different slip transmission behavior. To investigate the transmission behavior under these possible scenarios, we separately consider cases with the gliding dislocations on (111)-planes that intersect with the b_2 and b_3 boundary dislocations. Fig. 4 shows the results from both the MD-NVT and PFDD models of the dislocation-GB interaction when the initial gliding dislocation resides on b_2 and b_3 planes. In both cases, the leading partial dislocation directly transmits from its glide plane in Crystal 1 to the same glide plane in Crystal 2, in contrast to the glide dislocation initially located on b_1 plane. In the case of the b_3 plane, PFDD predicts transmission of both the leading and trailing partials but MD predicts transmission of only the leading partial. In all cases, Dislocation Extraction Algorithm (DXA) [84,85] identifies the transmitted dislocation to be $\frac{1}{6} < 112 >$ Shockley partial.

Fig. 5 also shows the transmission behavior of the leading and trailing partials in PFDD, however this figure presents a 1D evolution of the order parameters ξ_1 and ξ_3, colored by glide plane. This allows for a more quantitative view of the evolution of the order parameters in order to determine if the glide dislocation is indeed transmitting through the GB, or rather entering the GB and nucleating a new partial dislocation in Crystal 2. This plot corresponds to Figs. 3 and 4 by showing where the leading partials on each glide plane transmit across the GB. Each colored line represents a glide plane corresponding to a different boundary dislocation, and the plane on which the gliding dislocation is initiated is indicated with symbol 'x'. For example in the Fig. 5(a), the order parameter of leading partial initiates on b_1 glide plane, as indicated by the non-zero blue line, and then starts to evolve on b_3 plane, shown by the red line and indicating that the transmission plane is indeed the b_3 plane.

Fig. 5 provides detailed information about the transmission process in the GB region after the transmission event. We note that although the GB dislocations are fixed, the interaction of the leading partial with the GB dislocations is instead reflected in the evolution of the dislocation cores and stress state of the glide dislocations. Before crossing the GB (see the left side of GB), the order parameter evolves only on the glide plane for both leading and trailing partials. Once both leading and trailing partial dislocations on the b_1 plane reach the GB region under stress, the order pa-

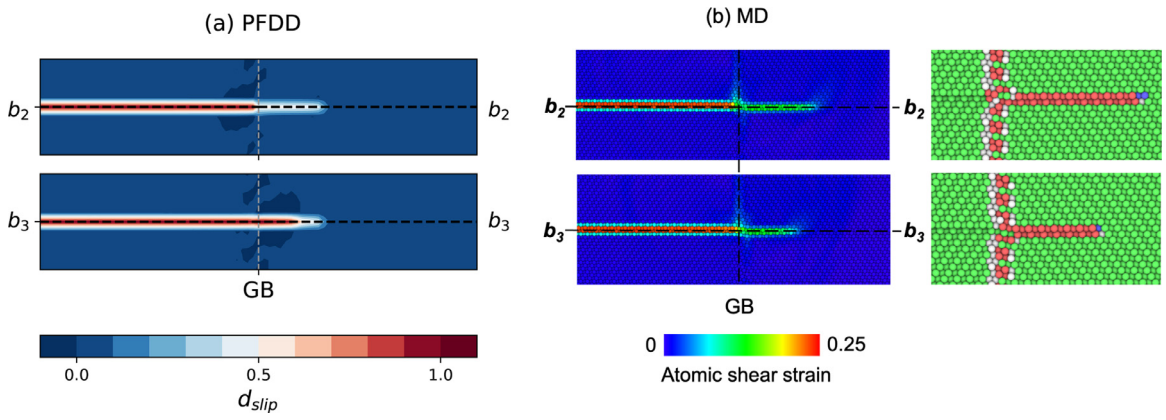

Fig. 4. (a) PFDD and (b) MD-NVT simulation results of dislocation transmission across the ITB when the gliding dislocation resides on the (top) b_2- and (bottom) b_3- plane, respectively. Also shown are the adaptive-CNA representations of atomic structure after transmission. Both MD and PFDD predict the leading partial on the b_2 plane will transmit onto the b_2 plane. For the b_3 plane, both the leading and trailing partials transmit onto the b_3 plane in PFDD, but only the leading partial transmits onto the b_3 plane in MD.

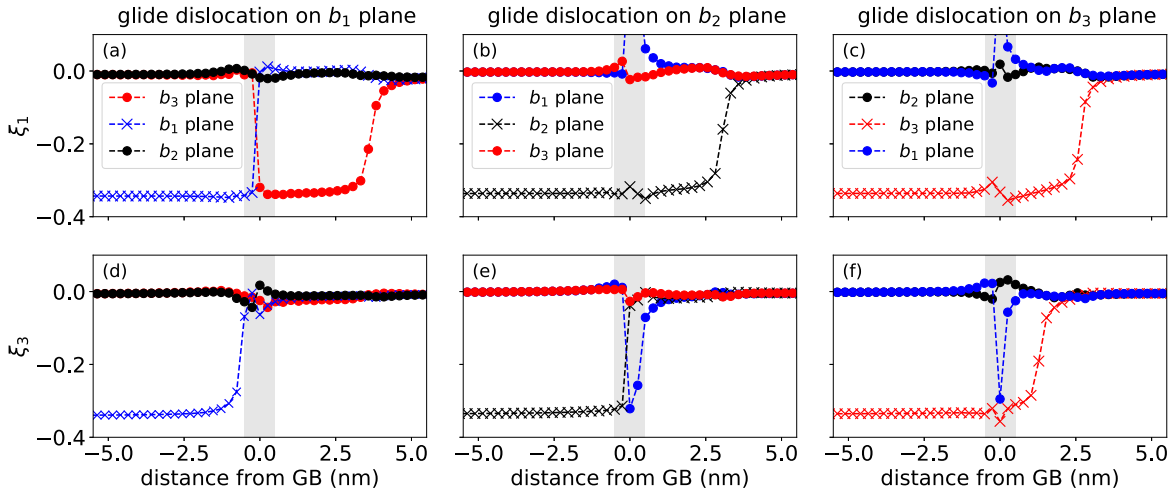

Fig. 5. The order parameters ξ_1 and ξ_3, which describe the leading (a,b and c) and trailing (d, e and f) partials, respectively, after the transmission event across the GB has occurred, computed using the elastically anisotropic PFDD model. Lines with the 'x' symbol indicate the plane on which the leading partial initiates and the adjacent planes (i.e., those associated with different boundary dislocations) are shown with solid symbols and different colors. The GB region is shown as a gray area. When the glide dislocation initiates on the b_1 or b_3 plane, slip is transferred to the b_3 plane in Crystal 2. On the other hand, glide dislocations initiated on the b_2 plane directly transmit onto the b_2 plane.

rameters ξ_1 and ξ_3 become zero (see Fig. 5(a) and (d)). Through linear combination with ξ_2 (not shown here), the Burgers vector of an initial perfect dislocation is left in the GB region on the (111) plane aligned with the b_1 boundary dislocation. Then, only a leading partial is nucleated and evolves on the b_3 plane in Crystal 2. When the initial glide dislocation is located on the b_2 plane (see Fig. 5(b) and (e)), the order parameter ξ_1 evolves in Crystals 1 and 2, crossing the GB, indicating that direct transmission occurred. On the b_2 plane, the ξ_3 parameter becomes zero at the boundary, indicating that the trailing partial arrests at the GB. For the b_3 glide plane (see Fig. 5(c) and (f)), both ξ_1 and ξ_3 evolve in Crystals 1 and 2, directly crossing the GB.

Note that there are non-zero order parameter values on the plane which is neither the initial glide plane nor the plane on which the leading partial has nucleated across the GB. For example, Fig. 5(b, c, e, f) shows non-zero order parameters on b_1 planes near the GB for both leading and trailing partials, and their linear combination does not represent either the perfect or partial dislocations predefined in this study. These non-zero order parameters remain the same as the leading partial evolves on the different planes. We attribute this behavior to elastic or plastic accommodation around ITB from interaction between the b_1 GB dislocation and glide dislocations. Also, it may induce other slip mechanisms such as cross-slip which is not incorporated in the current PFDD model.

It is worthwhile to compare our findings to previous MD studies and experiments on the transmission of glide dislocations across ITBs in Cu. For example, experimental studies on Cu from Li *et al.*[44,82] reported that when a 1/2< 110 > glide dislocation transmits across an ITB it can leave a sessile dislocation near the GB, which changes the local dislocation structure and leads to pinning of the ITB. While within the PFDD model we expect the Burgers vector of the transmitted dislocation to correspond to that of the impinging leading or trailing partials, our results do show similar behavior in that depending on the dislocation character of the gliding dislocation (either leading or trailing) and aligned GB dislocations, the trailing partial either transmits or is blocked by the GB. Although not shown here, in the latter case where trailing partial movement is blocked, we found that the stress state surrounding the GB is changed due to the presence of trailing partial, which may impact subsequent transmission behavior and thus, migration of ITB as suggested from previous studies. Liang *et al.*[35] had employed MD to study the transmission process of a screw dislocation across a Ni ITB considering different initial glide

Table 3
Critical transmission stress, τ, in units of MPa and transmission plane in Crystal 2 in parentheses of the leading glide partial dislocation computed using MD with two boundary conditions (MD-NVT and MD-NPT, see details in Section 2.1) and PFDD using anisotropic and isotropic elasticity, respectively. The critical stress is determined when the order parameter on any adjacent planes starts to evolve on the other side of the grain boundary continuously under stress.

Method	b_1	b_2	b_3
MD-NVT	547 ± 60 (b_3)	570 ± 62 (b_2)	328 ± 44 (b_3)
MD-NPT	$500 < \tau \leq 600$ (b_2)	$600 < \tau \leq 700$ (b_2)	$100 < \tau \leq 200$ (b_3)
PFDD (anisotropic)	$1104 < \tau \leq 1380$ (b_3)	$276 < \tau \leq 552$ (b_2)	$276 < \tau \leq 552$ (b_3)
PFDD (isotropic)	$276 < \tau \leq 552$ (b_3)	$138 < \tau \leq 276$ (b_2)	$276 < \tau \leq 552$ (b_3)

planes. They reported that the transmitted glide dislocation had the same screw sign as the incoming dislocation and emerges onto one plane (the b_2 plane) regardless of where the glide dislocation impinges. As just mentioned, the models here also predict that the same dislocation type exits the GB as the impinging dislocation, however, we find differences in the transmission plane using both MD and PFDD. This is possibly due to differences in the material γ-surface and related SFEs, and the applied stress state, which can impact the evolution and interaction of the gliding and GB dislocation cores. We also note that our MD simulations did not predict cross-slip. We attribute this to the fact that the stress state we considered is different from Liang *et al.* where they have additional stress components that result in non-zero resolved shear stresses on cross-slip planes. Thus, not accounting for cross-slip in the PFDD model is a reasonable assumption in this case.

3.3. Critical transmission stress

In addition to modeling the transmission process, we compared the MD and PFDD predictions for applied shear stress required for transmission through the boundary. Recall from Section 2.3, the critical transmission stress is determined to be in between the largest applied shear stress which does not cause transmission and the lowest stress required for the transmission event to occur. Table 3 shows the critical transmission stresses calculated with MD and PFDD for transmission events on the b_1-, b_2-, and b_3-planes. The table also shows the effect of MD boundary conditions and different treatments of elasticity within PFDD on the critical transmission stresses and planes.

Based on MD simulations with both boundary conditions, the transmission occurs under a similar range of stress magnitude for b_1 and b_2 cases while the transmission occurs at smaller stress for the b_3 case, which also shows differences between MD-NVT and MD-NPT. The transmission plane is dependent on the initial glide plane and shows good agreement between two boundary conditions for b_2- and b_3 cases. For the b_1 case from MD-NPT, we found that transmission occurs on two layers above the initial (111) plane, i.e., the b_2 plane, while MD-NVT predicts the transmission plane as one layer above, i.e., the b_3 plane. This indicates that different boundary conditions affect the stress state differently which yields larger/smaller climb forces (and possibly others as well) in transmission events.

On the other hand, the PFDD model predicts the same transmission planes when using either anisotropic or isotropic elasticity. However, the transmission stress values calculated with isotropic elasticity are lower for b_1- and b_2- cases while it is in the same range for the b_3 case. We note that we performed PFDD simulations using an elastically isotropic medium to better understand the transmission plane estimated from dislocation theory (which will be discussed in Section 4) and/or PFDD with anisotropic elasticity, not to directly compare to the critical transmission stress calculated with MD. Therefore, we compare the critical stresses computed from PFDD anisotropic calculations to the results from MD, which naturally accounts for anisotropic properties of materials.

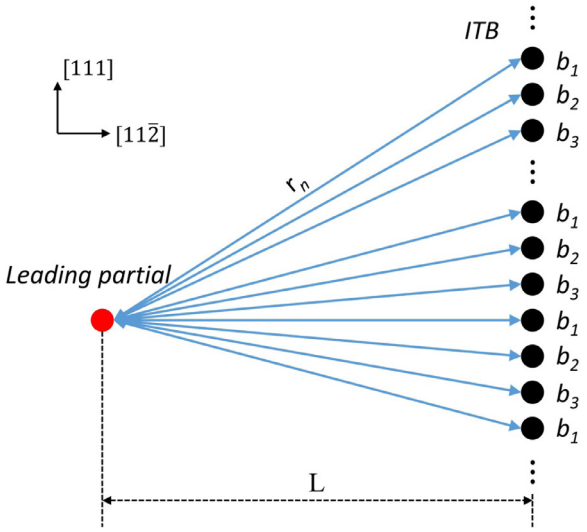

Fig. 6. Schematic of the leading partial dislocation interacting with an array of grain boundary dislocations as considered in Eq. (11).

In the case where the glide dislocation is aligned with b_2- and b_3- planes, PFDD and MD (MD-NVT in particular) show good agreement. However, for the case where the glide plane in Crystal 1 is aligned with the b_1 plane, PFDD overestimates the critical stress values by ~500 MPa. The possible reason for this large gap is that, besides all the differences between the MD and PFDD models, the b_1 GB dislocation is a pure edge dislocation which showed a relatively larger discrepancy in disregistry between PFDD and MD compared to the b_2 and b_3 cases (Fig. 2). Therefore, not allowing the GB to evolve in our PFDD modeling may have played a significant role during the transmission of the glide dislocation on the b_1 plane compared to other cases. Nevertheless, the overall match is reasonable considering PFDD does not account for short-range interactions between dislocation cores as MD does or changes in stress state as the dislocation interacts with the ITB.

4. Discussion

In order to understand the transmission phenomenon observed in MD and PFDD, we present an analytical argument using dislocation theory. Since the analytical solution is based on isotropic elasticity, we repeated the PFDD simulations using isotropic elasticity to better match predictions from dislocation theory and determine if there are any notable dependencies on anisotropic elasticity.

The force applied by the GB on the leading partial of the gliding dislocation can be calculated analytically using Eq. (11) [91]. In this calculation, the ITB is considered as an array of dislocations as shown in Fig. 6. The total force per unit length applied on the leading partial of the gliding dislocation is calculated as the sum of

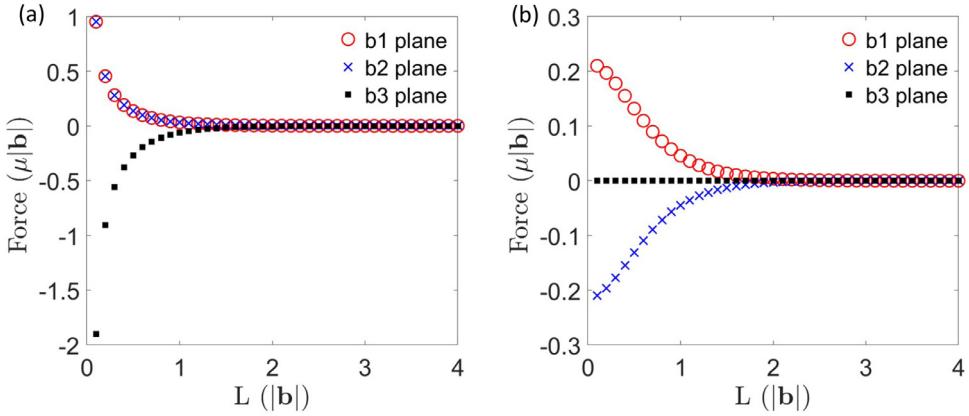

Fig. 7. Analytical calculation of the force applied by the GB dislocations (modeled as an array) on the leading partial of the gliding dislocation: (a) shows the in-plane force, and (b) shows the out-of-plane or climb force. Positive forces are repulsive, while negative forces are attractive.

the forces between the ITB dislocations and the leading partial,

$$F = \sum_n \left\{ \frac{\mu}{2\pi r_n} (\mathbf{b}_n^{GB} \cdot \zeta)(\mathbf{b}_{lp} \cdot \zeta) + \frac{\mu}{2\pi(1-\nu) r_n} [(\mathbf{b}_n^{GB} \times \zeta) \cdot (\mathbf{b}_{lp} \times \zeta)] \right\}, \quad (11)$$

where μ is the shear modulus, r_n is the distance between the leading partial and the n^{th} dislocation line in the ITB as shown in Fig. 6, $\mathbf{b}^{GB}$ and $\mathbf{b}_{lp}$ are Burgers vectors of the GB dislocations and the leading partial of gliding dislocation respectively, ζ is the dislocation line sense which is the same for all dislocations considered in this configuration, and ν is the Poisson's ratio.

Fig. 7(a) shows the in-plane force (i.e, along the glide plane in the $[11\bar{2}]$ direction) between the ITB and the leading partial. A positive force represents a repulsive interaction while a negative force indicates an attractive interaction. Clearly, the interaction on b_3 plane shows a significant attractive force when the leading partial moves close to the ITB. Thus, the critical stress for the transmission on b_3 plane should be small in comparison to the critical transmission stress required on the b_1 and b_2 planes, which is consistent with both MD and PFDD results as shown in Table 3. Fig. 7(b) shows the out-of-plane or climb force in the [111] direction between the ITB and the leading glide partial. On the b_1 (b_2) planes, this force is positive (negative) and indicates the leading partial will be 'pulled' to the plane that is above (below) the glide plane. This is consistent with the transmission of dislocation from b_1-plane to b_3-plane in MD-NVT and PFDD. However the leading partial moves up by two planes and transmits on the b_2-plane in MD-NPT. The out-of-plane force on b_3-plane is almost zero.

The combination of these two force components is expected to affect the critical stress and transmission plane. For example, when the gliding partial is on b_3 plane, there should be no out-of-plane forces acting on the dislocation during the transmission process and only an attractive in-plane force, hence we see a direct transmission mechanism. The leading partial on the b_1 and b_2 planes is influenced by both the repulsive in-plane and oppositely signed out-of-plane forces, contributing to larger critical transmission stresses compared to when the leading partial is on the b_3 plane and, in some cases, different transmission planes are observed. The analytical solutions are qualitatively consistent with our simulations and explain why we observe emergence on the b_3-plane when dislocation transmission occurs on b_1 plane, and a direct transmission mechanism on the b_3-plane. However, we observe different transmission behavior for the b_2 plane from both MD and PFDD simulations, where the transmission plane is the same as the glide plane, i.e., b_2 plane.

PFDD calculations using isotropic elasticity present similar results to those previously shown in Fig. 5. Many larger length scale models assume elastic isotropy to simplify calculations, and the effect of such assumptions must be carefully considered when bridging across scales. Overall, the transmission behavior is the same in all cases in that the transmission planes coincide with the results from MD-NVT and PFDD with using anisotropic elasticity. As shown in Table 3, the noticeable difference is that using isotropic elasticity tends to estimate lower (for b_1- and b_2 planes) or the same (for b_3 plane) critical transmission stress as compared to the simulations with anisotropic elasticity.

Considering that Eq. (11) is based on isotropic elasticity, the PFDD simulations that employ isotropic elasticity are expected to exhibit the same transmission plane as that predicted from dislocation theory (i.e., transmission to the b_3 plane for all cases). We indeed see agreement with dislocation theory for transmission on the b_1 and b_3 planes, and hence, this behavior appears to be well-described by the elastic interactions between the leading glide partial and the boundary misfit dislocations on these planes. In the case of transmission on the b_2 plane, all computational methods show direct transmission onto the b_2 plane, which is in contrast to what would be expected based on dislocation theory. The difference in predicted behavior is likely due to additional complex interactions that are captured in both PFDD and MD, but not in dislocation theory. For example, this analytical form does not consider the presence of the trailing partial dislocation or the stacking fault, which also may have played an role in transmission behavior of leading partial. Another example of this might be interactions between dislocation cores, which are naturally accounted for with MD. In our PFDD model, the GB dislocations do not evolve during the transmission process, indicating that the possible core changes from interactions are only captured through evolution of the glide dislocation. Based on our results, this treatment of the GB dislocations do not have an impact on the type of transmission, direct or indirect, observed, while it may have caused differences in transmission stresses.

5. Conclusions

To study the interaction between glide dislocations and a $\Sigma 3\{112\}$ ITB in Cu, we performed phase field dislocation dynamics (PFDD) and MD simulations. It has been previously shown that this ITB consists of a repeating triad of partial dislocations, denoted as b_1, b_2 and b_3 here [34]. Thus, in PFDD the GB is constructed as an array of repeating partial dislocations, and the disregistries of the misfit dislocations are shown to have good agreement with those calculated with MD. We studied the interaction of a glide disloca-

tion with each of the three misfit dislocations by investigating the transmission behavior when the glide dislocation impinges on different locations within the GB. In other words, the glide dislocation is located such that the glide plane is aligned with the different GB dislocations (i.e., the b_1-, b_2- or b_3 plane).

Our results show that the transmission plane and corresponding critical stresses depend on where the gliding dislocation impinges on the GB. Overall, the PFDD and MD results show good qualitative comparison. Quantitative differences are seen in the predictions for the critical stress values, where PFDD overpredicts the stress required for transmission on the b_1 plane, and produces values comparable to MD for the b_2 and b_3 planes. From both PFDD and MD calculations, the leading partial on the b_1 plane, is pulled upwards. Conversely, the leading partial on the b_2- and b_3 planes shows direct transmission behavior. To explain this behavior, we also performed theoretical analysis based on isotropic dislocation theory. Based on in-plane and out-of-plane forces exerted on the glide dislocation from the GB, dislocation theory predicts that all dislocations should transmit onto the b_3 plane. This is in agreement with the computational approaches for the b_1 and b_3 planes indicating that elastic interactions dominate this behavior. However, behavior predicted on the b_2 plane with PFDD and MD contradicts dislocation theory indicating that dislocation core interactions may play a larger role in this case.

Finally, we note that the PFDD model is not limited to describing this ITB and can be applied to various GBs comprised of misfit dislocations that can interact with one or multiple glide dislocations. However, the PFDD model does not yet account for climb along the GB interface or cross-slip behavior, and incorporating this phenomena would allow the model to capture more complex interaction behavior shown to occur by atomistic modeling.

This work presents direct comparison between the atomistic, mesoscale, and theoretical approaches to understand slip transfer across a GB. The comparison of transmission plane and critical transmission stress between PFDD and MD agree well, and the results indicate that ITBs can act as a barrier for screw dislocation motion. In particular, we found that the transmission behavior is dependent on the specific GB dislocation the gliding dislocation interacts with. This indicates that varying structure along a single GB may also impact the transmission behavior. We believe that this work conveys the transmission behavior observed from experiments and atomistic modeling, and will help to inform larger-scale modeling efforts.

Declaration of Competing Interest

The authors declare that they have no known competing financial interests or personal relationships that could have appeared to influence the work reported in this paper.

Acknowledgment

Simulations were performed using the CNLS clusters, the Darwin Computing Cluster and the HPC at Los Alamos National Laboratory (LANL). NM gratefully acknowledges support from the U.S. Department of Energy through the LANL/LDRD Program and the Center for Nonlinear Studies (CNLS) for this work. HK, NM, AH, and DJL gratefully acknowledge support from the Materials project within the Physics and Engineering Models (PEM) Subprogram element of the Advanced Simulation and Computing (ASC) Program at LANL. TM and LC acknowledge the financial support from National Science Foundation, Mechanics of Materials and Structures Program (Grant # 1727428). Los Alamos National Laboratory is operated by Triad National Security, LLC, for the National Nuclear Security Administration of U.S. Department of Energy (Contract No. 89233218CNA000001). This manuscript has been assigned LA-UR-21-23403. The authors also thank the anonymous reviewer for constructive comments on MD boundary conditions.

Appendix A. MD-NVT boundary condition

Fig. A.1 shows the evolution of stress state for MD-NVT simulations for the representative case of b_1 plane. Though the initial stress state was very close to the targeted state, we noticed that the $\sigma_{<111><110>}$ decreases and $\sigma_{<112><110>}$ increases once the dislocation gets close to the GB, possibly due to the GB-dislocation interaction. For the MD-NVT, the reported critical stress values in Table 3 are an average of $\sigma_{<111><110>}$ over the final 5 ps before the dislocation enters the ITB. The uncertainties on the reported values correspond to 1 standard deviation of the average.

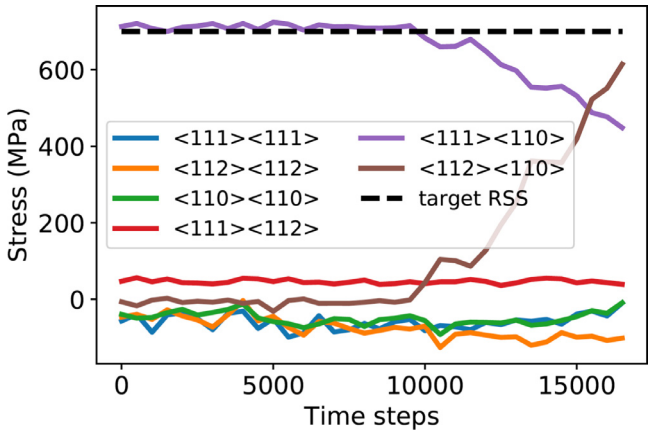

Fig. A.1. The evolution of the stress state for MD-NVT simulations as function of simulation time for the representative case of b_1 plane.

References

[1] J.P. Hirth, The influence of grain boundaries on mechanical properties, Metallurgical Transactions 3 (1972) 3047–3067.
[2] J.C.M. Li, Y.T. Chou, The role of dislocations in the flow stress grain size relationships, Metallurgical Transactions 1 (1970) 1145–1159.
[3] R.Z. Valiev, N.A. Enikeev, M.Y. Murashkin, V.U. Kazykhanov, X. Sauvage, On the origin of the extremely high strength of ultrafine-grained al alloys produced by severe plastic deformation, Scripta Materialia 63 (9) (2010) 949–952.
[4] V.Y. Gertsman, R. Birringer, H. Gleiter, R.Z. Valiev, On the structure and strength of ultrafine-grained copper produced by severe plastic deformation, Scripta metallurgica et materialia 30 (2) (1994).
[5] Y. Huang, T.G. Langdon, Advances in ultrafine-grained materials, Materials today 16 (3) (2013) 85–93.
[6] X. Li, Y. Wei, L. Lu, K. Lu, H. Gao, Dislocation nucleation governed softening and maximum strength in nano-twinned metals, Nature 464 (7290) (2010) 877–880.
[7] Q. An, W.A. Goddard III, Nanotwins soften boron-rich boron carbide ($B_{13}C_2$), Applied Physics Letters 110 (11) (2017) 111902.
[8] Q. An, W.A. Goddard III, K.Y. Xie, G.-d. Sim, K.J. Hemker, T. Munhollon, M.F. Toksoy, R.A. Haber, Superstrength through nanotwinning, Nano letters 16 (12) (2016) 7573–7579.
[9] W.Z. Abuzaid, M.D. Sangid, J.D. Carroll, H. Sehitoglu, J. Lambros, Slip transfer and plastic strain accumulation across grain boundaries in hastelloy X, Journal of the Mechanics and Physics of Solids 60 (2012) 1201–1220.
[10] D.E. Spearot, M.D. Sangid, Insights on slip transmission at grain boundaries from atomistic simulations, Current Opinion in Solid State & Materials Science 18 (2014) 188–195.
[11] Z.-H. Jin, P. Gumbsch, E. Ma, K. Albe, K. Lu, H. Hahn, H. Gleiter, The interaction mechanism of screw dislocations with coherent twin boundaries in different face-centred cubic metals, Scripta Materialia 54 (6) (2006) 1163–1168.
[12] J. Kacher, B.P. Eftink, B. Cui, I.M. Robertson, Dislocation interactions with grain boundaries, Current Opinion in Solid State & Materials Science 18 (2014) 227–243.
[13] E.O. Hall, The deformation and ageing of mild steel.3. discussion of results, Proceedings of the Physical Society of London Section B 64 (381) (1951) 747–753.
[14] N.J. Petch, Cleavage strength of polycrystals, J. Iron Steel Inst. 174 (Part 1) (1953) 25–28.

[15] L. Rémy, The interaction between slip and twinning systems and the influence of twinning on the mechanical behavior of fcc metals and alloys, Metallurgical Transactions A 12A (1981) 387–408.
[16] J.W. Christian, S. Mahajan, Deformation twinning, Progress in Material Sciences 39 (1995) 1–157.
[17] J. Chen, E.N. Hahn, A.M. Dongare, S.J. Fensin, Understanding and predicting damage and failure at grain boundaries in BCC Ta, Journal of Applied Physics 126 (2019) 165902.
[18] T.R. Bieler, P. Eisenlohr, F. Roters, D. Kumar, D.E. Mason, M.A. Crimp, D. Raabe, The role of heterogeneous deformation on damage nucleation at grain boundaries in single phase metals, International Journal of Plasticity 25 (9) (2009) 1655–1683.
[19] T. Nguyen, D.J. Luscher, J.W. Wilkerson, A dislocation-based crystal plasticity framework for dynamic ductile failure of single crystals, Journal of the Mechanics and Physics of Solids 108 (2017) 1–29.
[20] D.W. Lee, H. Kim, A. Strachan, M. Koslowski, Effect of core energy on mobility in a continuum dislocation model, Physical Review B 62 (2011) 3099–3108.
[21] Y. Zhu, H. Zhang, H. Wang, M. Suenaga, Grain boundary in textured $YBa_2Cu_3O_{7-\delta}$ superconductor, Journal of materials research 6 (12) (1991) 2507–2518.
[22] Y. Zhu, Y.L. Corcoran, M. Suenaga, Grain boundary chemistry and grain boundary dislocations in bulk $YBa_2Cu_3O_{7-\delta}$, Interface Science 1 (4) (1994) 361–370.
[23] V. Randle, The measurement of grain boundary geometry, IOP Publishing Ltd, Bristol, 1993.
[24] E. Bayerschen, A.T. McBride, B.D. Reddy, T. Böhlke, Review of slip transmission criteria in experiments and crystal plasticity models, Journal of Materials Science 51 (2016) 2243–2258.
[25] M.D. Sangid, H. Sehitoglu, H.J. Maier, T. Niendorf, Grain boundary characterization and energetics of superalloys, Materials Science and Engineering A 527 (2010) 7115–7125.
[26] J. Wang, N. Li, A. Misra, Structure and stability of Σ3 grain boundaries in face centered cubic metals, Philosophical Magazine 93 (4) (2013) 315–327.
[27] Y. Zhang, N.R. Tao, K. Lu, Effect of stacking-fault energy on deformation twin thickness in Cu–Al alloys, Scripta Materialia 60 (4) (2009) 211–213.
[28] N. Bernstein, E.B. Tadmor, Tight-binding calculations of stacking energies and twinnability in fcc metals, Physical Review B 69 (9) (2004) 094116.
[29] Z.H. Jin, P. Gumbsch, K. Albe, E. Ma, K. Lu, H. Gleiter, H. Hahn, Interaction between non-screw lattice dislocations and coherent twin boundaries in face–centered cubic metals, Acta Materialia 56 (2008) 1126–1135.
[30] T. Ezaz, M.D. Sangid, H. Sehitoglu, Energy barriers associated with slip-twin interactions, Philosophical Magazine 9 (10) (2011) 1464–1488.
[31] M. Chassagne, M. Legros, D. Rodney, Atomic-scale simulation of screw dislocation/coherent twin boundary interaction in Al, Au, Cu and Ni, Acta Materialia 59 (4) (2011) 1456–1463, doi:10.1016/j.actamat.2010.11.007.
[32] S. Xu, S.Z. Chavoshi, Y. Su, Deformation mechanisms in nanotwinned tungsten nanopillars: Effects of coherent twin boundary spacing, physica status solidi (RRL)–Rapid Research Letters 12 (3) (2018) 1700399.
[33] S. Xu, L. Xiong, Y. Chen, D.L. McDowell, Sequential slip transfer of mixed-character dislocations across Σ3 coherent twin boundary in FCC metals: a concurrent atomistic-continuum study, npj Computational Materials 2 (1) (2016) 1–9.
[34] J. Wang, O. Anderoglu, J.P. Hirth, A. Misra, X. Zhang, Dislocation structures of Σ 3 {112} twin boundaries in face centered cubic metals, Applied Physics Letters 95 (2009) 021908.
[35] Y. Liang, X. Yang, M. Gong, G. Liu, Q. Liu, J. Wang, Slip transmission for dislocations across incoherent twin boundary, Scripta Materialia 166 (2019) 39–43.
[36] Y. Liang, X. Yang, M. Gong, G. Liu, Q. Liu, J. Wang, Interactions between dislocations and three-dimensional annealing twins in face centered cubic metals, Computational Materials Science 161 (2019) 371–378.
[37] D. Bufford, Y. Liu, J. Wang, H. Wang, X. Zhang, *In situ* nanoindentation study on plasticity and work hardening in aluminum with incoherent twin boundaries, Nature Communications 5 (4864) (2014) 1–8.
[38] Y. Liu, J. Jian, Y. Chen, H. Wang, X. Zhang, Plasticity and ultra-low stress induced twin boundary migration in nanotwinned Cu by *in situ* nanoindentation studies, Applied Physics Letters 104 (2014) 231910.
[39] Q. Lu, Z. You, X. Huang, N. Hansen, L. Lu, Dependence of dislocation structure on orientation and slip systems in highly oriented nanotwinned Cu, Acta Materialia 127 (2017) 85–97, doi:10.1016/j.actamat.2017.01.016. https://www.sciencedirect.com/science/article/pii/S1359645417300265
[40] Y.T. Zhu, X.L. Wu, X.Z. Liao, J. Narayan, L.J. Kecskés, S.N. Mathaudhu, Dislocation-twin interactions in nanocrystalline fcc metals, Acta Materialia 59 (2) (2011) 812–821, doi:10.1016/j.actamat.2010.10.028. https://www.sciencedirect.com/science/article/pii/S1359645410006907
[41] J.B. Jeon, G. Dehm, Formation of dislocation networks in a coherent Cu ∑ 3(1 1 1) twin boundary, Scripta Materialia 102 (2015) 71–74, doi:10.1016/j.scriptamat.2015.02.016. https://www.sciencedirect.com/science/article/pii/S1359646215000706
[42] M. Chassagne, M. Legros, D. Rodney, Atomic-scale simulation of screw dislocation/coherent twin boundary interaction in Al, Au, Cu and Ni, Acta Materialia 59 (4) (2011) 1456–1463, doi:10.1016/j.actamat.2010.11.007. https://www.sciencedirect.com/science/article/pii/S1359645410007512
[43] L.L. Li, P. Zhang, Z.J. Zhang, Z.F. Zhang, Intrinsically higher fatigue cracking resistance of the penetrable and movable incoherent twin boundary, Scientific Reports 4 (3744) (2014) 1–5, doi:10.1038/srep03744.
[44] N. Li, J. Wang, J.Y. Huang, A. Misra, X. Zhang, Influence of slip transmission on the migration of incoherent twin boundaries in epitaxial nanotwinned Cu, Scripta Materialia 64 (2011) 149–152.
[45] Z.-H. Jin, P. Gumbsch, K. Albe, E. Ma, K. Lu, H. Gleiter, H. Hahn, Interactions between non-screw lattice dislocations and coherent twin boundaries in face–centered cubic metals, Acta Materialia 56 (5) (2008) 1126–1135.
[46] J. Wang, R.G. Hoagland, X.Y. Liu, A. Misra, The influence of interface shear strength on the glide dislocation–interface interactions, Acta Materialia 59 (8) (2011) 3164–3173.
[47] J. Wang, A. Misra, An overview of interface-dominated deformation mechanisms in metallic multilayers, Current Opinion in Solid State and Materials Science 15 (1) (2011) 20–28.
[48] A.H. Zahiri, P. Chakraborty, Y. Wang, L. Cao, Strong strain hardening in ultrafast melt-quenched nanocrystalline Cu: The role of fivefold twins, Journal of Applied Physics 126 (7) (2019) 075103.
[49] L. Lu, Y. Shen, X. Chen, L. Qian, K. Lu, Ultrahigh strength and high electrical conductivity in copper, Science 304 (5669) (2004) 422–426.
[50] K. Lu, L. Lu, S. Suresh, Strengthening materials by engineering coherent internal boundaries at the nanoscale, Science 324 (5925) (2009) 349–352.
[51] Y. Tian, B. Xu, D. Yu, Y. Ma, Y. Wang, Y. Jiang, W. Hu, C. Tang, Y. Gao, K. Luo, et al., Ultrahard nanotwinned cubic boron nitride, Nature 493 (7432) (2013) 385–388.
[52] J. Wang, N. Li, O. Anderoglu, X. Zhang, A. Misra, J.Y. Huang, J.P. Hirth, Detwinning mechanisms for growth twins in face-centered cubic metals, Acta Materialia 58 (2010) 2262–2270.
[53] M.P. Dewald, W.A. Curtin, Multiscale modelling of dislocation/grain-boundary interactions: I. Edge dislocations impinging on Σ11 (1 1 3) tilt boundary in Al, Modelling and Simulation in Materials Science and Engineering 15 (1) (2007) 192–215, doi:10.1088/0965-0393/15/1/S16.
[54] Y. Gao, Z. Jin, Interaction between lattice dislocations and low-angle grain boundaries in ni via molecular dynamics simulations, Molecular Simulation 43 (13-16) (2017) 1172–1178, doi:10.1080/08927022.2017.1356457.
[55] M.P. Dewald, W.A. Curtin, Multiscale modelling of dislocation/grain boundary interactions. II. screw dislocations impinging on tilt boundaries in Al, Philosophical Magazine 87 (30) (2007) 4615–4641, doi:10.1080/14786430701297590.
[56] M. Dewald, W.A. Curtin, Multiscale modeling of dislocation/grain-boundary interactions: III. 60° dislocations impinging on Σ3, Σ9 and Σ11 tilt boundaries in Al, Modelling and Simulation in Materials Science and Engineering 19 (5) (2011) 055002, doi:10.1088/0965-0393/19/5/055002.
[57] Z. Li, C. Hou, M. Huang, C. Ouyang, Strengthening mechanism in micro-polycrystals with penetrable grain boundaries by discrete dislocation dynamics simulation and hall-petch effect, Computational Materials Science 46 (4) (2009) 1124–1134, doi:10.1016/j.commatsci.2009.05.021. https://www.sciencedirect.com/science/article/pii/S0927025609002523
[58] B. Liu, D. Raabe, P. Eisenlohr, F. Roters, A. Arsenlis, G. Hommes, Dislocation interactions and low-angle grain boundary strengthening, Acta Materialia 59 (2011) 7125–7134.
[59] N. Verdhan, R. Kapoor, Interactions of dislocations with low angle tilt boundaries in fcc crystals, Computational Materials Science 98 (2015) 149–157.
[60] X. Zhang, S. Lu, B. Zhang, X. Tian, Q. Kan, G. Kang, Dislocation-grain boundary interaction-based discrete dislocation dynamics modeling and its application to bicrystals with different misorientations, Acta Materialia 202 (2021) 88–98.
[61] B. Liu, P. Eisenlohr, F. Roters, D. Raabe, Simulation of dislocation penetration through a general low-angle grain boundary, Acta Materialia 60 (2012) 5380–5390.
[62] Y. Zeng, A. Hunter, I.J. Beyerlein, M. Koslowski, A phase field dislocation dynamics model for a bicrystal interface system: An investigation into dislocation slip transmission across cube-on-cube interfaces, International Journal of Plasticity 79 (2016) 293–313.
[63] P. Zhao, C. Shen, M.F. Savage, J. Li, S.R. Niezgoda, M.J. Mills, Y. Wang, Slip transmission assisted by shockley partials across α/β interfaces in ti-alloys, Acta Materialia 171 (2019) 291–305.
[64] M. Koslowski, A. Cuitiño, M. Ortiz, A phase-field theory of dislocations dynamics, strain hardening and hysteresis in ductile single crystals, Journal of the Mechanics and Physics of Solids 50 (12) (2002) 2597–2635.
[65] Y.U. Wang, Y.M. Jin, A.M. Cuitiño, A.G. Khachaturyan, Nanoscale phase field microelasticity theory of dislocations: model and 3d simulations, Acta Materialia 49 (2001) 1847–1857.
[66] J.R. Mianroodi, B. Svendsen, Atomistically determined phase-field modeling of dislocation dissociation, stacking fault formation, dislocation slip, and reactions in fcc systems, Journal of the Mechanics and Physics of Solids 77 (2015) 109–122.
[67] S. Plimpton, Fast parallel algorithms for short-range molecular dynamics, Journal of Computational Physics 117 (1995) 1–19. Also see http://lammps.sandia.gov/
[68] Y. Mishin, M.J. Mehl, D.A. Papaconstantopoulos, A.F. Voter, J.D. Kress, Structural stability and lattice defects in copper: Ab initio, tight-binding, and embedded-atom calculations, Physical Review B 63 (22) (2001) 2241061–22410616, doi:10.1103/PhysRevB.63.224106.
[69] V. Vitek, Intrinsic stacking faults in body-centered cubic crystals, Phil. Mag. 18 (154) (1968) 773–786.
[70] M.S. Duesbery, V. Vitek, Plastic anisotropy in b.c.c. transition metals, Acta Materialia 46 (5) (1998) 1481–1492, doi:10.1016/S1359-6454(97)00367-4. http://www.sciencedirect.com/science/article/pii/S1359645497003674

[71] S.M. Rassoulinejad-Mousavi, Y. Mao, Y. Zhang, Evaluation of copper, aluminum, and nickel interatomic potentials on predicting the elastic properties, Journal of Applied Physics 119 (24) (2016) 244304, doi:10.1063/1.4953676.
[72] M.A. Tschopp, S.P. Coleman, D.L. McDowell, Symmetric and asymmetric tilt grain boundary structure and energy in Cu and Al (and transferability to other fcc metals), Integrating Materials and Manufacturing Innovation 4 (1) (2015) 11, doi:10.1186/s40192-015-0040-1.
[73] I.J. Beyerlein, A. Hunter, Understanding dislocation mechanics at the mesoscale using phase field dislocation dynamics, Philosophical Transactions of the Royal Society A 374 (2016) 20150166.
[74] S. Xu, Y. Su, I.J. Beyerlein, Modeling dislocations with arbitrary character angle in face-centered cubic transition metals using the phase-field dislocation dynamics method with full anisotropic elasticity, Mechanics of Materials 139 (2019) 103200.
[75] S. Xu, J.R. Mianroodi, A. Hunter, I.J. Beyerlein, B. Svendsen, Phase-field-based calculations of the disregistry fields of static extended dislocations in FCC metals, Philosophical Magazine 99 (11) (2019) 1400–1428.
[76] J.R. Mianroodi, A. Hunter, I.J. Beyerlein, B. Svendsen, Theoretical and computational comparison of models for dislocation dissociation and stacking fault/core formation in fcc systems, Journal of the Mechanics and Physics of Solids 95 (2016) 719–741.
[77] G. Schoeck, The core structure, recombination energy and peierls energy for dislocations in Al, Philosophical Magazine A 81 (5) (2001) 1161–1176.
[78] C. Shen, Y. Wang, Incorporation of γ-surface to phase field model of dislocation: simulating dislocation dissociation in fcc crystals, Acta Materialia 52 (2004) 683–691.
[79] A. Hunter, R.F. Zhang, I.J. Beyerlein, The core structure of dislocation and their relationship to the material γ-surface, Journal of Applied Physics 115 (2014) 134314.
[80] A. Hunter, I.J. Beyerlein, T.C. Germann, M. Koslowski, Infuence of the stacking fault energy surface on partial dislocations in fcc metals with a three-dimensional phase field model, Physical Review B 84 (144108) (2011) 1–10.
[81] L. Cao, M. Koslowski, Rate-limited plastic deformation in nanocrystalline Ni, Journal of Applied Physics 117 (24) (2015) 244301.
[82] N. Li, J. Wang, X. Zhang, A. Misra, In-situ TEM study of dislocation-twin boundaries interaction in nanotwinned Cu films, Jom 63 (9) (2011) 62.
[83] N. Lu, K. Du, L. Lu, H.Q. Ye, Motion of 1/3< 111> dislocations on $\sum${112} twin boundaries in nanotwinned copper, Journal of Applied Physics 115 (2) (2014) 024310.
[84] A. Stukowski, K. Albe, Extracting dislocations and non-dislocation crystal defects from atomistic simulation data, Modelling and Simulation in Materials Science and Engineering 18 (8) (2010) 085001, doi:10.1088/0965-0393/18/8/085001. http://stacks.iop.org/0965-0393/18/i=8/a=085001?key=crossref.b09a8081fb2d4aa0f81d8e5e945e6c1a
[85] A. Stukowski, V.V. Bulatov, A. Arsenlis, Automated identification and indexing of dislocations in crystal interfaces, Modelling and Simulation in Materials Science and Engineering 20 (8) (2012) 085007, doi:10.1088/0965-0393/20/8/085007.
[86] J. Wang, R.G. Hoagland, J.P. Hirth, A. Misra, Atomistic simulations of the shear strength and sliding mechanisms of copper-niobium interfaces, Acta Materialia 56 (13) (2008) 3109–3119, doi:10.1016/j.actamat.2008.03.003. https://www.sciencedirect.com/science/article/pii/S1359645408001900
[87] S. Xu, J.R. Mianroodi, A. Hunter, I.J. Beyerlein, B. Svendsen, Phase-field-based calculations of the disregistry fields of static extended dislocations in FCC metals, Philosophical Magazine 99 (11) (2019) 1400–1428.
[88] L. Cao, A. Hunter, I.J. Beyerlein, M. Koslowski, The role of partial mediated slip during quasi-static deformation of 3d nanocrystalline metals, Journal of the Mechanics and Physics of Solids 78 (2015) 415–426.
[89] M.L. Falk, J.S. Langer, Dynamics of viscoplastic deformation in amorphous solids, Phys. Rev. E 57 (1998) 7192–7205, doi:10.1103/PhysRevE.57.7192.
[90] F. Shimizu, S. Ogata, J. Li, Theory of shear banding in metallic glasses and molecular dynamics calculations, MATERIALS TRANSACTIONS 48 (11) (2007) 2923–2927, doi:10.2320/matertrans.MJ200769.
[91] P.M. Anderson, J.P. Hirth, J. Lothe, Theory of dislocations, Cambridge University Press, 2017.